

# Channel Measurements and Characterization with Phase Drift Compensation for Outdoor 330-360 GHz MIMO Communications

Tian Qiu, Taihao Zhang, Cunhua Pan, *Senior Member, IEEE*, Hong Ren, *Member, IEEE*, Yongchao He, Chenzhou Lin, Bingchang Hua, and Jiangzhou Wang, *Fellow, IEEE*

**Abstract**—In this paper, an outdoor channel measurement campaign at 330-360 GHz employing a  $128 \times 4$  virtual antenna array (VAA)-based multiple-input multiple-output (MIMO) configuration is conducted. The transmitter (Tx) and receiver (Rx) location pairs are classified into line-of-sight (LoS) and obstructed-LoS (OLoS) scenarios to enable a detailed investigation of outdoor terahertz (THz) band channel characteristics. During the measurement process, the stationarity of the outdoor environment is carefully verified, and a linear phase drift (PD) effect is identified. Then, we propose a PD-aware Space-Alternating Generalized Expectation-Maximization (SAGE) algorithm, which significantly improves both delay resolution and channel parameter estimation accuracy. Based on the processed measurement data, we characterize key channel properties, including the power delay profile, path loss, shadow fading, delay spread, angular spread, Rician K-factor, as well as their cumulative distribution functions and correlation characteristics. In addition, near-field effects and MIMO-specific properties, including the spatial non-stationarity and the cluster birth-death property, are analyzed.

**Index Terms**—Terahertz, Channel measurement, MIMO, PD-aware SAGE

## I. INTRODUCTION

TERAHERTZ (THz) communication is widely recognized as a key enabling technology for sixth-generation (6G) wireless communications, offering abundant spectrum resources to alleviate the spectrum scarcity and capacity limitations of current wireless systems [1], [2]. Channel measurements and characterization are essential for understanding propagation mechanisms and provide a fundamental basis for system design and deployment [3], [4]. Therefore, to fully exploit the potential of the THz band, channel measurement campaigns in representative scenarios are necessary [5], [6].

Since channel characteristics strongly depend on the operating frequency range, propagation environment, and deployment scenario, dedicated channel measurement campaigns must be conducted in representative scenarios of interest. Indoor THz channel measurements have been extensively investigated. In [7], sub-THz channel characterization and modeling were performed for indoor industrial scenarios based on radio propagation measurements at 142 GHz in four factories, where 82 transmitter-receiver (Tx-RX) locations under both line-of-sight (LoS) and non-LoS (NLoS) conditions were selected and more than 75,000 spatial and temporal channel impulse

responses were collected. In [8], indoor channel measurement campaigns were conducted at 201-209 GHz, covering four communication scenarios, including a meeting room, cubicle area, hallway, and an NLoS case. In [9], small-scale fading (SSF) channel characterization and sparsity analysis were performed based on vector network analyzer (VNA)-based measurements in typical indoor scenarios, including a narrow corridor and a semi-open hall, at 215-225 GHz. In [10], an indoor channel measurement campaign at 260-400 GHz was reported using a 128-element virtual multi-antenna linear array, thereby improving the understanding of THz multi-antenna channel characteristics.

In addition to conventional indoor scenarios, several special scenarios have also been investigated. In [11], a measurement campaign was carried out in a real aircraft to investigate the radio channel at 300 GHz for different deployments of a wireless in-flight entertainment (IFE) system. In [12], a comprehensive comparison and analysis of channel characteristics at 28 GHz, 38 GHz, and 130 GHz were also presented based on extensive measurements conducted in an aircraft cabin. In [13], the smart rail mobility channel at the 300 GHz band was characterized using ultra-wideband (UWB) channel sounding and ray tracing (RT) with an 8 GHz bandwidth. Five scenarios were considered, including train-to-infrastructure (T2I), inside-station, train-to-train (T2T), infrastructure-to-infrastructure (I2I), and intra-wagon scenarios. The corresponding channel characteristics were then extracted and analyzed. In [14], THz channel performance under snowy conditions was comprehensively investigated through a combination of outdoor measurements and advanced channel modeling techniques. To further expand the understanding of THz-band channels, outdoor channel measurement campaigns remain indispensable.

### A. Related Work

1) *THz-band Outdoor Channel Measurement*: Recently, considerable efforts have been devoted to outdoor THz channel measurements. At 142 GHz, NYU WIRELESS conducted a series of outdoor urban microcell (UMi) measurement studies for sub-THz channel characterization [15]–[18]. Specifically, [15] investigated the spatial autocorrelation properties of three critical channel parameters, namely shadow fading (SF), delay spread (DS), and angular spread (AS). In [16], outdoor omnidirectional and directional path loss (PL) models were provided for both LoS and NLoS scenarios, along with an analysis of foliage loss, i.e., signal attenuation caused by foliage. In [17], the channel spatial statistics, including the number of spatial clusters and the cluster power distribution, were studied. Based on the derived empirical channel

Tian Qiu, Taihao Zhang, Cunhua Pan, Hong Ren, Yongchao He, Chenzhou Lin and Jiangzhou Wang are with National Mobile Communications Research Laboratory, Southeast University, Nanjing, China (e-mail: tianqiu, taihao, cpan, hren, heyongchao, 213223687, j.z.wang@seu.edu.cn).

Bingchang Hua is with Institution: Purple Mountain Laboratories, Nanjing, Jiangsu 211111, China (e-mail: huabingchang@pmlabs.com.cn).

Corresponding author: Cunhua Pan.

statistics, a detailed spatial statistical multiple-input multiple-output (MIMO) channel generation procedure was further introduced. Building upon these measurement efforts, [18] summarized extensive measurement results and statistical analyses to formulate a multiband empirical three-dimensional (3-D) statistical channel model (SCM) for outdoor urban open square and street scenarios. [19] conducted wideband channel measurements in an outdoor street canyon environment around the 300 GHz band and investigated several key channel parameters. The analysis of PL and root mean square (RMS) DS showed that outdoor environments exhibit more severe large-scale fading and greater delay domain dispersion. In [20], wideband channel measurements were conducted in an L-shaped university campus street at 306-321 GHz and 356-371 GHz. Specifically, 10 LoS and 8 NLoS measurement points were considered for the two frequency bands. The results verified the sparsity of multipath components (MPCs) at THz frequencies and showed smaller power spreads in both the temporal and spatial domains in the THz band. [21] and [22] conducted channel measurements and statistical modeling at 145-146 GHz for urban device-to-device (D2D) and UMi environments, respectively, using VNA-based channel sounders. These studies investigated key channel parameters and provided statistical models that enable a more realistic and detailed performance assessment of THz communication systems. Nevertheless, comprehensive outdoor THz-band MIMO channel measurements and characterization remain insufficiently investigated.

2) *Stationarity Verification*: Many existing measurement studies assume that the channel environment is quasi-static or semi-static [15], [23], without explicitly verifying its stationarity. However, in virtual antenna array (VAA) measurements, the extended acquisition duration may introduce phase drift (PD) errors and potential channel variations. In [24], the authors pointed out that time-division multiplexed (TDM) and VAA sounders are susceptible to phase-noise-induced measurement errors, and demonstrated through theoretical analysis and simulations that local oscillator (LO) impairments can lead to significant errors in MIMO channel capacity estimation. In [25], the short-term phase noise of TDM-based channel sounders was further investigated, and its impact on MIMO channel capacity estimation was evaluated. In [26], reference antenna measurements were used to estimate and correct PD errors during post-processing, and an iterative low-complexity CLEAN algorithm was adopted for MPC extraction in outdoor-to-indoor (O2I) urban macrocell (UMa) and UMi. Nevertheless, stationarity verification and PD compensation for VNA-based VAA MIMO measurements in the THz band remain relatively underexplored.

3) *Measurement Data Processing Methods*: The Space-Alternating Generalized Expectation-Maximization (SAGE) algorithm was originally proposed as a generalization of the classical expectation-maximization (EM) algorithm [27]. By alternating among multiple hidden-data spaces and updating only a subset of the parameter vector in each iteration, SAGE can accommodate smoothness penalties and achieve faster convergence than conventional EM algorithms. In [28], the SAGE algorithm was applied to mobile radio channel measurements

under both synthetic and real-world conditions, demonstrating its effectiveness in the high-resolution extraction of MPC parameters. Owing to its high resolution and iterative refinement capability, SAGE has been widely adopted for wireless channel parameter estimation [23].

## B. Contributions

To address the aforementioned gaps, we conduct outdoor MIMO channel measurements in the 330-360 GHz band. The main contributions of this paper are summarized as follows:

- We conduct outdoor THz-band MIMO channel measurements using a VAA configuration. Based on the measured data, we characterize key channel characteristics, including the power delay profile (PDP), PL, SF, DS, AS, Rician K-factor (KF), along with their cumulative distribution functions (CDFs) and correlation properties. Moreover, the Kolmogorov-Smirnov (KS) test is performed to evaluate the goodness of fit between the empirical CDFs and several candidate statistical distributions.
- In addition, near-field effects and MIMO-specific properties, including the spatial non-stationarity (SnS) and the cluster birth-death property, are analyzed.
- We identify the inherent PD in the outdoor VAA-based measurement data and demonstrate that it can be effectively characterized using linear fitting. Based on this observation, a PD-aware SAGE algorithm is proposed as a post-processing method for channel parameter extraction. Compared with the PD-unaware algorithm, the proposed method significantly improves both delay resolution and overall estimation accuracy, as demonstrated by the simulation and measurement results.
- For outdoor channel characterization, we classify the measured TRx locations into LoS and obstructed-LoS (OLoS) cases and perform a comparative analysis of their channel characteristics. The results reveal the impact of obstruction on various channel characteristics in THz band.

## C. Organization and Notation

The remainder of this paper is organized as follows. Section II describes the measurement environment and system setup. Section III presents the stationarity verification and the proposed PD-aware SAGE algorithm. The outdoor MIMO channel characteristics and modeling results are analyzed in Section IV. Finally, Section V concludes the paper.

*Notations*: Boldface lowercase  $\mathbf{x}$  and uppercase  $\mathbf{X}$  denote vectors and matrices with  $[\mathbf{x}]_m$  and  $[\mathbf{X}]_{m,n}$  denoting the  $m$ -th and  $(m,n)$ -th entry of  $\mathbf{x}$  and  $\mathbf{X}$ , respectively. For a matrix  $\mathbf{X}$  of arbitrary size, the symbols  $\mathbf{X}^*$ ,  $\mathbf{X}^T$ , and  $\mathbf{X}^H$  represent the conjugate, transpose, and conjugate transpose  $\mathbf{X}$ , respectively. The modulus of a scalar is denoted by  $|\cdot|$ , the Euclidean norm of vector  $\mathbf{x}$  is denoted by  $\|\mathbf{x}\|_2$ , and the Frobenius norm of matrix  $\mathbf{X}$  is denoted by  $\|\mathbf{X}\|_F$ . The vectorization operator  $\text{vec}(\mathbf{X})$  stacks the columns of  $\mathbf{X}$  into a column vector, whereas  $\text{mat}(\mathbf{X})$  reshapes  $\mathbf{X}$  into a matrix of specified dimensions following column-wise ordering. The expectation operator is denoted by  $\mathbb{E}[\cdot]$ . Additionally, the Kronecker product and transposed Khatri-Rao product between two matrices  $\mathbf{X}$  and  $\mathbf{Y}$  are denoted by  $\mathbf{X} \otimes \mathbf{Y}$  and  $\mathbf{X} \bullet \mathbf{Y}$ , respectively.

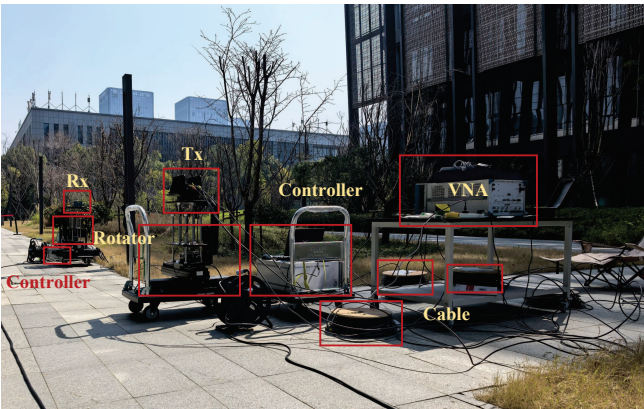
## II. OUTDOOR MIMO CHANNEL MEASUREMENT

In this section, the empirical outdoor measurement campaign conducted in the 330-360 GHz band is presented. To capture the spatial characteristics of outdoor THz propagation, a  $128 \times 4$  VAA-based MIMO configuration is employed. The measurement campaign is designed to support the analysis of both large-scale and small-scale channel characteristics, as well as MIMO-specific propagation phenomena. In the following, we first describe the outdoor measurement environment and the classification of TRx links, and then introduce the VNA-based measurement system and its key configuration parameters.

### A. Measurement Environment

The 330-360 GHz outdoor measurement campaign is conducted in a rectangular street area at Purple Mountain Laboratories (PML), Nanjing, as shown in Fig. 1. Specifically, Fig. 1 (a) presents a photograph of the measurement environment, while Fig. 1 (b) illustrates the corresponding layout, including the Tx and Rx locations as well as the positions of the main objects in the environment. For notational simplicity, the links between Tx location 1 and Rx locations 1-8 are denoted as TRx locations 1-8, while those from Tx location 2 to Rx locations 8-1 are denoted as TRx locations 9-16. The central grassland is approximately 0.6 m in height, while the shrubs and trees are approximately 1.4 m and 3 m tall, respectively. Based on the blockage caused by shrubs and trees, TRx1-TRx5, TRx8-TRx10, and TRx14-TRx16, corresponding to 11 locations, are classified as LoS cases, whereas TRx6-TRx7 and TRx11-TRx13, corresponding to 5 locations, are classified as OLoS cases.

VAA has been demonstrated as a promising technique for measuring high-frequency multi-antenna channels [10], [29]–[31]. To realize the MIMO measurement, a VAA configuration is adopted, in which the Tx and Rx antenna elements are sequentially moved to predefined spatial sampling locations. Specifically, high-precision motorized linear stages are used to synthesize ULA layouts at both the Tx and Rx sides, with  $N_T = 128$  and  $N_R = 4$ , respectively. At each movement step, the antenna is displaced by half the wavelength corresponding to the center frequency, thereby satisfying spatial sampling requirements for the synthesized virtual arrays.



(a) Measurement environment.

### B. Measurement System Setup

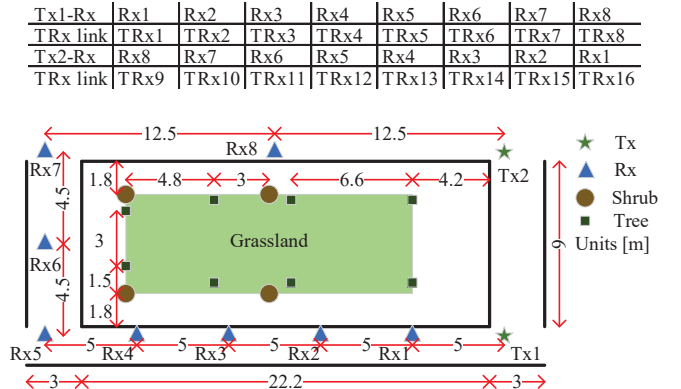
TABLE I  
MEASUREMENT SYSTEM SETUP

Parameter	Value	Parameter	Value
Start frequency	330 GHz	End frequency	360 GHz
Time domain resolution	33.33 ps	Bandwidth	30 GHz
Path length resolution	1 cm	IFBW	1 kHz
Maximum excess delay	166.67 ns	Sweeping points	5001
Maximum path length	49.97 m	Sweeping interval	6 MHz
Antenna gain at Tx	25 dBi	HPBW of Tx	10°
Antenna gain at Rx	25 dBi	HPBW of Rx	10°
Average noise floor	-145 dBm	Test power	0.5 mW

The outdoor MIMO channel measurements in the THz band are conducted using a VNA-based frequency-domain measurement system operating in the 330-360 GHz band. The detailed operating principle of the measurement system can be found in [10]. As shown in Fig. 1 (a), in the transmitter module, the VNA generates a radio frequency (RF) signal spanning 12.22-13.33 GHz, which is up-converted by a  $\times 27$  frequency multiplier (FM). Meanwhile, a LO generates a signal over 13.75-15 GHz, which is up-converted by a  $\times 24$  FM. The two resulting signals are then mixed to generate a 279 MHz intermediate-frequency (IF) reference signal. An analogous process is performed in the receiver module to generate the corresponding test signal. The key system configuration parameters and measurement setup are summarized in Table I.

### III. STATIONARITY VERIFICATION AND PD-AWARE SAGE ALGORITHM

Most existing channel measurement studies assume that the propagation environment remains quasi-static during the measurement process [15], [23]; however, this assumption is seldom verified experimentally, especially for VAA-based THz MIMO measurements, where the sequential antenna movement leads to an extended acquisition duration. In such measurements, even if the physical environment is approximately static, hardware-related impairments may introduce PD [24], which can distort the measured channel responses and bias



(b) Measurement layout.

Fig. 1. Outdoor THz-band MIMO channel (a) measurement environment and (b) layout.

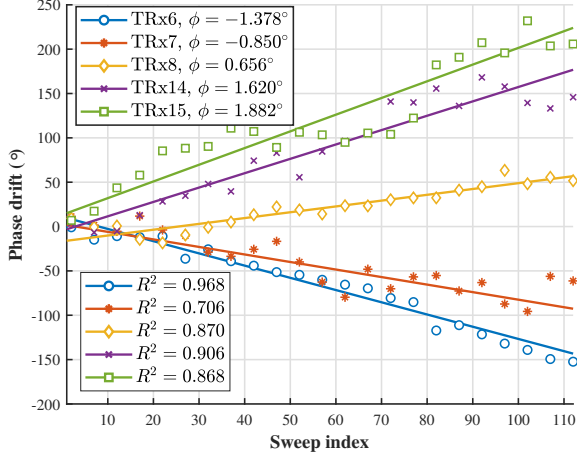


Fig. 2. Linear PD fitted results.

the subsequent MPC parameter estimation. Therefore, before extracting channel characteristics, it is necessary to examine the temporal stationarity of the measurement environment. In this section, we first verify the stationarity of the measurement environment and reveal the existence of an approximately linear PD. Based on this observation, we further propose a PD-aware SAGE algorithm that incorporates PD compensation into the iterative MPC extraction process, thereby improving the reliability and resolution of channel parameter estimation.

#### A. Linear PD

Several TRx location pairs are selected to verify the environmental stationarity. Specifically, during the verification, the Tx at the 128-th antenna element and the Rx at the 4-th antenna element are placed in a face-to-face configuration with their boresight directions aligned and are kept stationary. Multiple frequency sweep measurements are then performed under the same system configuration described in Section II-B.

By plotting the measured phase against the sweep index, which characterizes the temporal evolution of the measurement, it is observed that the PD exhibits an approximately linear trend, while the measured amplitude remains nearly constant. Therefore, linear fitting is performed on the measured phase data, and the corresponding results are shown in Fig. 2, where the straight lines denote the fitted results and the markers denote the measured data. The goodness of fit is quantified by the coefficient of determination, which is calculated as

$$R^2 = 1 - \frac{\sum_{i=1}^N (\varphi_i - \hat{\varphi}_i)^2}{\sum_{i=1}^N (\varphi_i - \bar{\varphi})^2}, \quad (1)$$

where  $\varphi_i$ ,  $\hat{\varphi}_i$ , and  $\bar{\varphi}$  denote the measured phase drift, fitted phase drift, and mean measured phase drift, respectively, and  $N$  denotes the total number of sweeps. The obtained  $R^2$  values have an average of 0.864, indicating that the linear model effectively captures the dominant temporal trend of the PD during the measurement process. As indicated by the fitting results, the slope represents the PD, denoted by  $\phi$ . The prior information extracted from the fitted results is further utilized in the design of the subsequent PD-aware SAGE algorithm.

#### B. PD-aware SAGE algorithm

The VNA measures and records the scattering parameters. By applying amplitude and phase calibration, the effects of the system frequency response are removed. The calibrated frequency-domain response between the  $t$ -th Tx antenna element and the  $r$ -th Rx antenna element at the  $k$ -th frequency point is given by

$$H^{(r,t)}[k] = \frac{S_{21}^{(r,t)}[k]}{H_{\text{RF}}^{\text{Tx}}[k]H_{\text{device}}[k]H_{\text{RF}}^{\text{Rx}}[k]}, \quad (2)$$

where  $1 \leq k \leq K$ .  $H_{\text{RF}}^{\text{Tx}}[k]$  and  $H_{\text{RF}}^{\text{Rx}}[k]$  denote the frequency responses of the RF front ends at the Tx and Rx, respectively, and  $H_{\text{device}}[k]$  accounts for the frequency response contributions from the VNA and cables. Finally,  $H^{(r,t)}[k]$  represents the calibrated channel frequency response (CFR). By arranging  $H^{(r,t)}[k]$  over all Rx-Tx antenna element pairs, the MIMO CFR matrix under the VAA configuration is obtained as

$$\mathbf{H}[k] = \sqrt{\frac{N_R N_T}{L}} \sum_{l=1}^L \alpha_l e^{-j2\pi k \Delta f \tau_l} \mathbf{a}_{N_R}(\psi_l) \mathbf{a}_{N_T}^H(\omega_l), \quad (3)$$

where  $[\alpha_l, \tau_l, \psi_l, \omega_l]$  denotes the complex path gain, delay, angle of arrival (AoA), and angle of departure (AoD) of the  $l$ -th MPC, respectively.  $\Delta f$  is the frequency sweep interval.  $\mathbf{a}_{N_R}(\psi_l) \in \mathbb{C}^{N_R \times 1}$  and  $\mathbf{a}_{N_T}(\omega_l) \in \mathbb{C}^{N_T \times 1}$  denote the array response vectors (ARVs) at the Rx and Tx, respectively, and are given by

$$\mathbf{a}_{N_R}(\psi_l) = \frac{1}{\sqrt{N_R}} e^{-j\frac{2\pi}{\lambda_c} d_R \sin(\psi_l)} [0, 1, \dots, N_R - 1]^T, \quad (4a)$$

$$\mathbf{a}_{N_T}(\omega_l) = \frac{1}{\sqrt{N_T}} e^{-j\frac{2\pi}{\lambda_c} d_T \sin(\omega_l)} [0, 1, \dots, N_T - 1]^T, \quad (4b)$$

where  $\lambda_c$ ,  $d_R$ , and  $d_T$  denote the carrier wavelength, Rx antenna spacing, and Tx antenna spacing, respectively.

Next, we incorporate the linear PD observed in Section III-A into the channel model. The PD-aware CFR matrix, denoted by  $\mathbf{H}_{\text{pd}}[k] = \mathbf{H}[k]e^{jk\phi}$ , is expressed as

$$\mathbf{H}_{\text{pd}}[k] = \sum_{l=1}^L \tilde{\alpha}_l e^{-j2\pi k \Delta f (\tau_l - \frac{\phi}{2\pi \Delta f})} \mathbf{a}_{N_R}(\psi_l) \mathbf{a}_{N_T}^H(\omega_l), \quad (5)$$

where  $\tilde{\alpha}_l \triangleq \sqrt{\frac{N_R N_T}{L}} \alpha_l$  denotes the equivalent path gain<sup>1</sup>. As can be observed from Eq. (5), the effective delay becomes  $\tilde{\tau}_l \triangleq \tau_l - \frac{\phi}{2\pi \Delta f}$ . Therefore, failure to properly account for PD will result in biased delay estimates, which may consequently degrade the estimation accuracy of other channel parameters.

Moreover, the CFR in Eq. (5) can be expressed in a compact matrix form as

$$\mathbf{H}_{\text{pd}}[k] = \mathbf{A}_{N_R} \mathbf{\Lambda} \mathbf{A}_{N_T}^H, \quad (6)$$

where  $\mathbf{A}_{N_R} = [\mathbf{a}_{N_R}(\psi_1), \dots, \mathbf{a}_{N_R}(\psi_L)] \in \mathbb{C}^{N_R \times L}$  and  $\mathbf{A}_{N_T} = [\mathbf{a}_{N_T}(\omega_1), \dots, \mathbf{a}_{N_T}(\omega_L)] \in \mathbb{C}^{N_T \times L}$  denote the

<sup>1</sup>In practical channel measurement processing, the normalization factor  $\sqrt{\frac{N_R N_T}{L}}$  is omitted. In addition, the carrier-frequency-dependent phase term associated with  $f_c$ , which should be included in Eq. (3), is also absorbed into the equivalent complex path gain during parameter extraction and does not affect the subsequent analysis.

AoA and AoD steering matrices, respectively, and  $\mathbf{\Lambda}[k] = \text{Diag}(\tilde{\alpha}_1 e^{-j2\pi k \Delta f \tilde{\tau}_1}, \dots, \tilde{\alpha}_L e^{-j2\pi k \Delta f \tilde{\tau}_L}) \in \mathbb{C}^{L \times L}$  denotes the frequency-dependent equivalent complex gain matrix.

The EM-based SAGE algorithm is widely used for the offline processing of large-scale channel measurement data [23]. Unlike the conventional EM algorithm, which relies on a single complete-data space and updates all parameters simultaneously, SAGE alternates among multiple admissible hidden-data spaces and updates only a subset of the parameter vector in each iteration by maximizing the corresponding objective function. In practical channel parameter estimation, this maximization step can be implemented using high-resolution parameter estimation techniques. Building upon this framework, we propose a PD-aware SAGE algorithm to jointly refine the MPC parameters and compensate for measurement-induced PD. The proposed algorithm follows a SAGE-based iterative estimation structure, where each path component is updated through an orthogonal matching pursuit (OMP)-type procedure.

In the expectation-step (**E-step**), the admissible hidden data associated with the  $l$ -th MPC are constructed by subtracting the currently reconstructed contributions of all other MPCs from the received matrix, i.e.,

$$\hat{\mathbf{H}}_{\text{pd}}^l[k] = \mathbf{H}[k] - \sum_{l'=1, l' \neq l}^{\hat{L}} \hat{\mathbf{H}}_{\text{pd}}^{l'}[k], \quad 1 \leq k \leq K. \quad (7)$$

In the maximization steps (**M-steps**),  $\text{OMP}(\mathbf{Y}, \mathbf{A}, J)$  denotes a  $J$ -sparse signal recovery problem, where  $\mathbf{Y}$  is the observation matrix,  $\mathbf{A}$  is the corresponding sensing dictionary, and  $J$  is the sparsity level. In the following, we detail the construction of the observation matrices and sensing matrices for estimating each MPC parameter. The complete PD-aware SAGE procedure is summarized in Algorithm 1.

Let the PD-aware delay response vector of the  $l$ -th MPC be defined as

$$\mathbf{t}_{\text{pd}}(\tilde{\tau}_l) = [e^{-j2\pi \Delta f \tilde{\tau}_l}, \dots, e^{-j2\pi K \Delta f \tilde{\tau}_l}]^T \in \mathbb{C}^{K \times 1}. \quad (8)$$

By vectorizing the  $l$ -th path component at each frequency point and concatenating the results over frequency, the  $l$ -th PD-aware delay observation matrix is constructed as

$$\mathbf{Y}_{\tau_l} \triangleq \left[ \text{vec}(\hat{\mathbf{H}}_{\text{pd}}^l[1]), \dots, \text{vec}(\hat{\mathbf{H}}_{\text{pd}}^l[K]) \right]^T \\ \approx \tilde{\alpha}_l \mathbf{t}_{\text{pd}}(\tilde{\tau}_l) (\mathbf{a}_{N_T}^*(\omega_l)) \otimes \mathbf{a}_{N_R}(\psi_l)^T \in \mathbb{C}^{K \times N_R N_T}. \quad (9)$$

To estimate the delay with high precision while reducing computational complexity, the dominant delay window is identified from the CIR obtained by inverse fast Fourier transform (IFFT). Specifically, for the  $(r, t)$ -th Rx-Tx antenna element pair, the corresponding  $l$ -th equivalent single-input single-output (SISO) frequency-domain response is given by

$$(\hat{\mathbf{h}}_{\text{pd}}^l)^{(r,t)} \triangleq \left[ [\hat{\mathbf{H}}_{\text{pd}}^l[1]]_{r,t}, \dots, [\hat{\mathbf{H}}_{\text{pd}}^l[K]]_{r,t} \right] \\ \approx \tilde{\alpha}_l [\mathbf{a}_{N_R}(\psi_l)]_r [\mathbf{a}_{N_T}^*(\omega_l)]_t \mathbf{t}_{\text{pd}}(\tilde{\tau}_l) \in \mathbb{C}^{K \times 1}. \quad (10)$$

Thus, the average PDP (APDP) of the  $l$ -th MPC, denoted by  $\text{APDP}_l$ , is obtained by averaging the PDPs reconstructed from the  $l$ -th MPC over all Rx-Tx antenna element pairs. Specifically,

the reconstructed CIR for the  $(r, t)$ -th antenna element pair is given by

$$(\hat{\mathbf{c}}_{\text{pd}}^l)^{(r,t)} = \text{IFFT}((\hat{\mathbf{h}}_{\text{pd}}^l)^{(r,t)}) \in \mathbb{C}^{K \times 1}. \quad (11)$$

Then,  $\text{APDP}_l$  is computed as

$$\text{APDP}_l = \frac{1}{N_R N_T} \sum_{r=1}^{N_R} \sum_{t=1}^{N_T} \left| (\hat{\mathbf{c}}_{\text{pd}}^l)^{(r,t)} \right|^2. \quad (12)$$

The dominant delay window is then identified as the location with the maximum value of it and a local delay grid  $\tau_l = [\tau_{l,1}, \dots, \tau_{l,D_{\tau_l}}] \in \mathbb{C}^{1 \times D_{\tau_l}}$  is constructed, where  $D_{\tau_l}$  denotes the delay dictionary size. The corresponding delay sensing matrix is given by

$$\mathbf{A}_{\tau_l} = [e^{-j2\pi \Delta f}, \dots, e^{-j2\pi K \Delta f}]^T \otimes \tau_l \in \mathbb{C}^{K \times D_{\tau_l}}. \quad (13)$$

Constructing  $\mathbf{A}_{\tau_l}$  only within the dominant delay window improves delay resolution while reducing the search complexity<sup>2</sup>.

After obtaining the coarse delay estimate  $\hat{\tau}_l^c$ , the PD-aware sensing matrix is constructed to jointly refine the delay and PD estimates. Specifically, a local refined delay sensing matrix  $\mathbf{A}_{\hat{\tau}_l}$  is constructed around the coarse estimate  $\hat{\tau}_l^c$ . Let  $\phi = [\phi_1, \dots, \phi_{D_\phi}] \in \mathbb{C}^{1 \times D_\phi}$  denote the PD search grid, whose range is determined using the prior information obtained in Section III-A and  $D_\phi$  denotes the dictionary size. The corresponding PD sensing matrix is defined as

$$\mathbf{A}_{\text{pd}} = [e^{j1}, \dots, e^{jK}]^T \otimes \phi \in \mathbb{C}^{K \times D_\phi}. \quad (14)$$

Thus, the joint sensing matrix is constructed as  $\mathbf{A}_{\hat{\tau}_l} \bullet \mathbf{A}_{\text{pd}}$ .

After the refined delay  $\hat{\tau}_l^r$  and PD estimates  $\hat{\phi}$  are obtained, the corresponding PD-aware delay atom is reconstructed as  $\mathbf{t}_{\text{pd}}(\hat{\tau}_l)$ . For angle-domain parameter estimation, the delay-domain influence is eliminated by projecting  $\mathbf{Y}_{\tau_l}$  onto the estimated PD-aware delay response vector. The  $l$ -th AoA observation matrix is then constructed by reordering the projected spatial-domain response into an  $N_R \times N_T$  matrix as

$$\mathbf{Y}_{R_l} \triangleq \text{mat} \left( \frac{\mathbf{t}_{\text{pd}}^H(\hat{\tau}_l) \mathbf{Y}_{\tau_l}}{K} \right) \approx \mathbf{a}_{N_R}(\psi_l) (\tilde{\alpha}_l \mathbf{a}_{N_T}^H(\omega_l)). \quad (15)$$

To estimate  $l$ -th AoA  $\psi_l$ , the Rx-side sensing dictionary is constructed as

$$\mathbf{A}_R = [\mathbf{a}_{N_R}(-1), \mathbf{a}_{N_R}(-1 + 2/D_R), \dots, \mathbf{a}_{N_R}(1 - 2/D_R)], \quad (16)$$

where  $D_R \geq N_R$  denotes the dictionary size and the grid resolution is  $2/D_R$ . Similarly, the  $l$ -th AoD observation matrix is constructed as

$$\mathbf{Y}_{T_l} \triangleq \left( \mathbf{Y}_{R_l} \right)^H \approx \mathbf{a}_{N_T}(\omega_l) (\tilde{\alpha}_l^* \mathbf{a}_{N_R}^H(\psi_l)) \in \mathbb{C}^{N_T \times N_R}. \quad (17)$$

The  $l$ -th AoD  $\omega_l$  can be estimated in the same manner using the Tx-side sensing dictionary  $\mathbf{A}_T$ <sup>3</sup>.

<sup>2</sup>In measurement data processing, the measured PDP can be directly obtained from the data. Therefore, the delay window range can be manually fine-tuned to achieve higher-precision delay estimation.

<sup>3</sup>The order of delay-domain and angle-domain parameter estimation is not fixed and can be adjusted according to their relative influence on the overall estimation accuracy. For example,  $\mathbf{Y}_{R_l}$  can be constructed before delay estimation as  $\mathbf{Y}_{R_l} \triangleq \left[ \hat{\mathbf{H}}_{\text{pd}}^l[1], \dots, \hat{\mathbf{H}}_{\text{pd}}^l[K] \right] \approx \mathbf{a}_{N_R}(\psi_l) (\tilde{\alpha}_l \mathbf{t}_{\text{pd}}^T(\tilde{\tau}_l) \otimes \mathbf{a}_{N_T}^H(\omega_l)) \in \mathbb{C}^{N_R \times K N_T}$ .

---

**Algorithm 1** PD-Aware SAGE Algorithm
 

---

**Input:**  $\mathbf{H}_{\text{pd}}[k]$ ,  $1 \leq k \leq K$ ; stopping threshold  $\epsilon$ ; maximum number of iterations  $\delta_{\text{max}}$ ; sensing matrices  $\{\mathbf{A}_{\text{pd}}, \mathbf{A}_R, \mathbf{A}_T\}$ ; estimated number of MPCs  $\widehat{L}$ .

- 1: **Initialization:** Set  $\text{NMSE}^{(0)} = 0$  and iteration index  $\delta = 1$ . Initialize  $\{\widehat{\mathbf{H}}_{\text{pd}}^l[k]\}_{l=1}^{\widehat{L}}$  and compute  $\text{NMSE}^{(1)}$ .
- 2: **while**  $|\text{NMSE}^{(\delta)} - \text{NMSE}^{(\delta-1)}| > \epsilon$  and  $\delta < \delta_{\text{max}}$  **do**
- 3:    $\delta \leftarrow \delta + 1$
- 4:   **for**  $1 \leq l \leq \widehat{L}$  **do**
- 5:     **E-step:**  $\widehat{\mathbf{H}}_{\text{pd}}^l[k] = \mathbf{H}[k] - \sum_{l'=1, l' \neq l}^{\widehat{L}} \widehat{\mathbf{H}}_{\text{pd}}^{l'}[k]$ .
- 6:     Obtain  $\mathbf{Y}_{\tau_l}$  via Eq. (9).
- 7:     Obtain  $\widehat{\mathbf{h}}_{\text{pd}}^{l,(r,t)}$  via Eq. (10).
- 8:     Obtain  $\tau_l$  from APDP<sub>*l*</sub>.
- 9:     Construct the coarse delay sensing matrix  $\mathbf{A}_{\tau_l}$ .
- 10:    **M-step:**  $\widehat{\tau}_l^c = \text{OMP}(\mathbf{Y}_{\tau_l}, \mathbf{A}_{\tau_l}, 1)$ .
- 11:    Construct the local refined delay sensing matrix  $\mathbf{A}_{\widehat{\tau}_l}$ .
- 12:    **M-step:**  $(\widehat{\tau}_l', \widehat{\phi}) = \text{OMP}(\mathbf{Y}_{\tau_l}, \mathbf{A}_{\widehat{\tau}_l} \bullet \mathbf{A}_{\text{pd}}, 1)$ .
- 13:    Obtain  $\mathbf{Y}_{R_l}$  via Eq. (15).
- 14:    **M-step:**  $\widehat{\psi}_l = \text{OMP}(\mathbf{Y}_{R_l}, \mathbf{A}_R, 1)$ .
- 15:    Obtain  $\mathbf{Y}_{T_l} = (\mathbf{Y}_R^l)^H$ .
- 16:    **M-step:**  $\widehat{\omega}_l = \text{OMP}(\mathbf{Y}_{T_l}, \mathbf{A}_T, 1)$ .
- 17:    **M-step:**  $\widehat{\mathbf{a}}_l = \mathbf{a}_{N_R}(\widehat{\psi}_l)^H \mathbf{Y}_{R_l} \mathbf{a}_{N_T}(\widehat{\omega}_l)$ .
- 18:    Update the estimated *l*-th PD-aware MPC  $\widehat{\mathbf{H}}_{\text{pd}}^l[k]$ .
- 19:    **end for**
- 20:    Update the estimated CFR as  $\widehat{\mathbf{H}}_{\text{pd}}[k] = \sum_{l=1}^{\widehat{L}} \widehat{\mathbf{H}}_{\text{pd}}^l[k]$ .
- 21:    Compute  $\text{NMSE}^{(\delta)}$ .
- 22: **end while**

**Output:**  $\{\widehat{\omega}_l, \widehat{\tau}_l, \widehat{\psi}_l, \widehat{\omega}_l\}_{l=1}^{\widehat{L}}, \widehat{\phi}, \widehat{\mathbf{H}}_{\text{pd}}[k]$ ,  $1 \leq k \leq K$ .

---

Then, by exploiting the approximate orthogonality of the large-scale array response vectors, the equivalent complex path gain  $\alpha_l$  is estimated as  $\widehat{\alpha}_l = \mathbf{a}_{N_R}(\widehat{\psi}_l)^H \mathbf{Y}_{R_l} \mathbf{a}_{N_T}(\widehat{\omega}_l)$ .

In the proposed algorithm,  $\widehat{L}$  is predefined to be sufficiently large to ensure that all significant propagation paths in the measurement data can be captured. This overcomplete setting is commonly adopted for measured channels [23], where the exact number of MPCs is unknown in advance. However, because  $\widehat{L}$  is intentionally selected to be large, some estimated components may correspond to weak or negligible paths. Although PD affects all MPCs,  $\phi$  is not estimated uniformly after all  $\widehat{L}$  path components have been updated, since including these weak components in a global PD estimation may introduce additional errors and degrade the estimation accuracy. Instead, the PD estimation is incorporated into the path-wise refinement process, where the delay and PD are jointly estimated based on the corresponding dominant hidden-data component.

Moreover, proper initialization can accelerate convergence. This can be achieved by performing the M-steps once, or by applying the multiple signal classification (MUSIC) algorithm [28], before iterative refinement. For example, solving the OMP problem associated with Eq. (6) with sparsity level  $L$  yields the initial estimates  $\{\widehat{\psi}_l\}_{l=1}^{\widehat{L}}$ .

Fig. 3 (a) illustrates the simulation-based validation of the proposed PD-aware SAGE algorithm. In the simulation, the received signal is modeled as  $\mathbf{Y}[k] = \sqrt{p}\mathbf{H}_{\text{pd}}[k] + \mathbf{N}[k]$ , where  $p$  denotes the transmit power and  $\mathbf{N}[k]$  denotes additive

white Gaussian noise (AWGN). The Tx and Rx are equipped with ULAs consisting of  $N_T = 64$  and  $N_R = 64$  antenna elements, respectively. The antenna spacings are set to  $d_T = d_R = \lambda_c/2$ , where  $\lambda_c$  denotes the wavelength corresponding to the center frequency. The complex path gains are modeled as  $\alpha_l \sim \mathcal{CN}(0, 10^{-3}d_{\text{TR}}^{-2.2})$ , where  $d_{\text{TR}} = 50$  m denotes the Tx-Rx distance. The noise power is set to  $\sigma^2 = -80$  dBm. The dictionary sizes are set to  $D_R = N_R$  and  $D_T = N_T$ , and  $\psi_l$  and  $\omega_l$  are randomly generated from the corresponding angular grids. In addition, the propagation distance corresponding to each delay is uniformly generated within  $\mathcal{U}[5, 15]$  m. The PD  $\phi$  is uniformly sampled from  $[0.4^\circ, 5^\circ]$ . The remaining parameters are set consistently with those of the measurement system. For comparison, the PD-unaware baseline omits the construction of the joint PD-aware sensing matrix and does not estimate  $\phi$ . Since the ground-truth CFR  $\mathbf{H}_{\text{pd}}[k]$  is unavailable for actual measurement data, the NMSE is computed as follows

$$\text{NMSE} = \mathbb{E} \left\{ \frac{\sum_{k=1}^K \left\| \widehat{\mathbf{H}}_{\text{pd}}[k] - \mathbf{Y}[k] \right\|_F^2}{\sum_{k=1}^K \left\| \mathbf{Y}[k] \right\|_F^2} \right\}. \quad (18)$$

As observed from the figure, increasing the number of MPCs  $L$  degrades the estimation accuracy due to the larger number of unknown parameters. A larger PD  $\phi$  also affects the estimation performance, particularly for the PD-unaware baseline. This is because  $\phi$  not only introduces bias into the delay estimation but also affects the selection of the dominant signal window. When  $\phi$  is large, the effective delay  $\widehat{\tau}_l$  may be shifted outside the selected window, resulting in severe estimation errors. In contrast, the proposed PD-aware SAGE algorithm consistently outperforms the PD-unaware baseline, and the performance gap becomes more pronounced as  $p$  increases.

The proposed PD-aware algorithm is then applied to the measured data<sup>4</sup>. For the  $(r, t)$ -th Rx-Tx antenna element pair, the reconstructed CIR is obtained by applying the IFFT to the sum of all estimated MPC CFRs, i.e.,

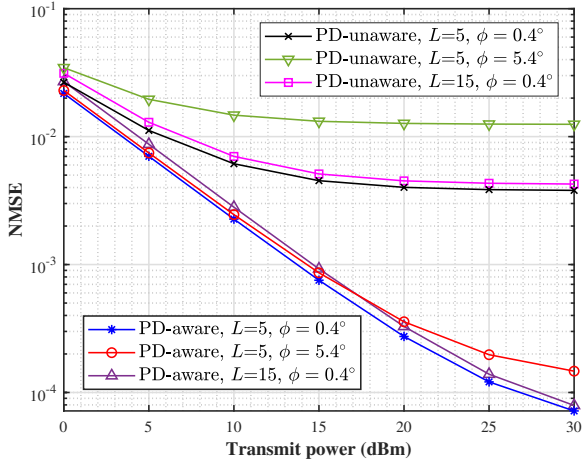
$$\mathbf{c}^{(r,t)} = \text{IFFT} \left( \sum_{l=1}^L (\mathbf{h}^l)^{(r,t)} \right) \in \mathbb{C}^{K \times 1}. \quad (19)$$

The corresponding PDP is given by the squared magnitude of the CIR. The APDP is then computed by averaging the PDPs over all Rx-Tx antenna element pairs as

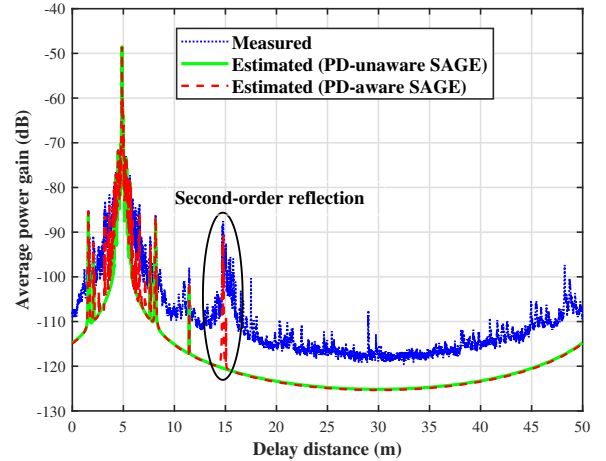
$$\text{APDP} = \sum_{l=1}^L \text{APDP}_l = \frac{1}{N_R N_T} \sum_{r=1}^{N_R} \sum_{t=1}^{N_T} \left| \mathbf{c}^{(r,t)} \right|^2. \quad (20)$$

Fig. 3 (b) presents the measurement-based validation of the proposed PD-aware SAGE algorithm using the data measured at the TRx1 location. As observed, the PD-aware algorithm improves the delay-domain resolution. Specifically, both the PD-aware and PD-unaware algorithms can identify the LoS path at approximately 5 m, whereas only the PD-aware algorithm successfully resolves the second-order reflection path caused by the measurement devices at approximately 15 m. The averaged

<sup>4</sup>For notational simplicity, the estimation marker  $\widehat{\cdot}$  and the subscript pd are omitted in the following sections unless otherwise specified.



(a) Simulation-based validation, with  $\hat{L} = L$ ,  $\delta_{\max} = 5$ , and  $\epsilon = 10^{-6}$ .



(b) Measurement-based validation, with  $\hat{L} = 100$ ,  $\delta_{\max} = 5$ , and  $\epsilon = 10^{-4}$ .

Fig. 3. Validation of the proposed PD-aware SAGE algorithm.

NMSE values over all Rx-Tx antenna element pairs are calculated as  $\text{NMSE}_{\text{aware}} = \frac{1}{N_R N_T} \sum_{r=1}^{N_R} \sum_{t=1}^{N_T} \text{NMSE}_{\text{aware}}^{(r,t)} = 0.0164$  and  $\text{NMSE}_{\text{unaware}} = 0.0390$ , respectively. In addition, the relative NMSE reduction is first computed for each Rx-Tx antenna element pair and then averaged over all pairs, yielding an average improvement of 61.571%.

#### IV. CHANNEL CHARACTERIZATION AND MODELING

This section presents a comprehensive characterization and modeling of the measured outdoor THz-band MIMO channels. The stationarity analysis in Section III confirms the validity of extracting channel characteristics from the measurement data, thereby supporting reliable MPC parameter estimation. Based on the processed channel responses and extracted MPC parameters, both large-scale and small-scale channel characteristics are analyzed, including path loss (PL), shadow fading (SF), delay spread (DS), angular spread (AS), Rician K-factor (KF), and correlation properties. In addition, near-field effects and MIMO-specific propagation phenomena, such as spatial non-stationarity (SnS) and cluster birth-death property, are investigated to provide a more complete understanding of outdoor THz MIMO propagation. A comparative analysis between LoS and OLoS cases is also conducted to reveal the impact of vegetation obstruction on the measured channel characteristics. Table II summarizes the measurement and fitting results for the selected channel parameters, where the blue-highlighted TRx locations correspond to LoS cases and the yellow-highlighted TRx locations correspond to OLoS cases.

##### A. APDP

As an example, the measured and estimated APDPs at the TRx1 location are shown in Fig. 3(b). The estimated results match well with the measured data, indicating that most MPCs are accurately extracted, although some weak paths with large delays are not detected. A strong LoS path is observed, with

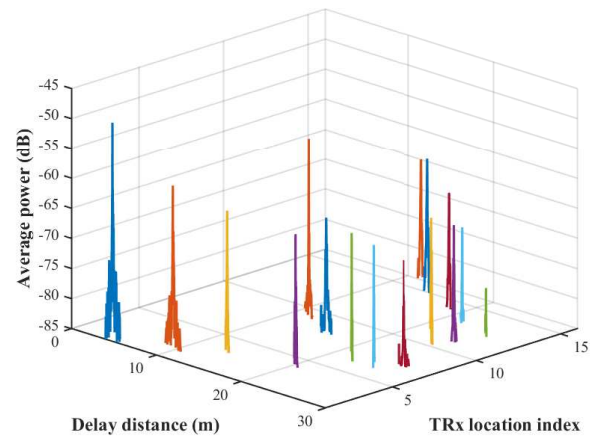


Fig. 4. APDP evolution across TRx locations

an average power gain of  $-48.528$  dB, whereas the second-order reflection path has an average power gain of  $-90.675$  dB. Moreover, the spurious peaks near the path (SPNP) phenomenon has been discussed in detail in our previous work [10].

Fig. 4 shows the APDP evolution across the 16 TRx locations. The APDPs exhibit a sparse multipath structure, with received power mainly concentrated in a few dominant delay components. This behavior is consistent with the propagation characteristics of the THz band. For LoS cases, the strongest APDP peak generally corresponds to the direct path, and its delay distance closely follows the Tx-Rx distance. For OLoS cases, the dominant component may arise from a residual direct component through partially blocked vegetation, foliage-induced scattering, or edge diffraction effects.

TABLE II  
MEASUREMENT RESULTS AND SUMMARY OF CHANNEL PARAMETERS

TRx location	1	2	3	4	5	6	7	8	9	10	11	12	13	14	15	16	
PL	PL (dB)	91.986	104.666	110.813	117.220	120.120	120.283	120.184	112.835	107.356	119.902	120.034	129.474	121.438	115.735	110.271	110.066
	CI model	$n_{LoS} = 2.443, n_{OLOS} = 2.778$															
	FI model	$\alpha_{LoS} = 3.905, \beta_{LoS} = 65.810, \alpha_{OLOS} = 3.508, \beta_{OLOS} = 72.916$															
SF	CI model (dB)	-8.007	-2.982	-0.719	1.961	2.696	-2.120	-2.941	0.116	-2.293	2.686	-2.172	6.446	0.760	1.405	-0.184	0.975
	FI model (dB)	-0.660	-0.215	-0.277	0.174	-0.388	-2.145	-3.156	-0.152	-0.724	-0.273	-2.145	6.257	1.189	0.173	-0.535	2.878
	$\sigma_{SF}$ (dB)	$\sigma_{SF,LoS}^{CI} = 3.034$ dB, $\sigma_{SF,OLOS}^{CI} = 3.464$ dB, $\sigma_{SF,LoS}^{FI} = 0.952$ dB, $\sigma_{SF,OLOS}^{FI} = 3.456$ dB															
DS	$\sigma_r$ (ns)	0.606	0.755	0.362	1.023	0.244	0.227	0.665	0.656	0.245	0.446	0.549	0.610	0.330	0.405	0.425	0.456
	LN ( $\log_{10}(DS/1ns)$ )	$\mu_{DS} = -0.348, \sigma_{DS} = 0.197$															
AS	$\sigma_\omega$ (°)	3.768	2.351	2.893	1.972	2.418	4.353	3.187	1.732	2.850	4.288	5.651	-	5.658	4.309	5.505	-
	LN ( $\log_{10}(AS/1^\circ)$ )	$\mu_{AS} = 0.512, \sigma_{AS} = 0.218$															
KF	$\mu_\kappa$ (dB)	14.528	7.730	15.876	13.035	18.655	19.728	9.275	8.933	21.117	14.097	12.019	11.393	19.658	16.037	15.305	14.279
	$\sigma_\kappa$ (dB)	5.290	1.608	2.889	0.934	0.986	1.052	0.917	0.692	3.204	1.111	1.372	1.529	3.789	1.459	1.859	1.102
	LN ( $\log_{10}(\kappa)$ )	$\mu_{KF} = 1.448, \sigma_{KF} = 0.449$															

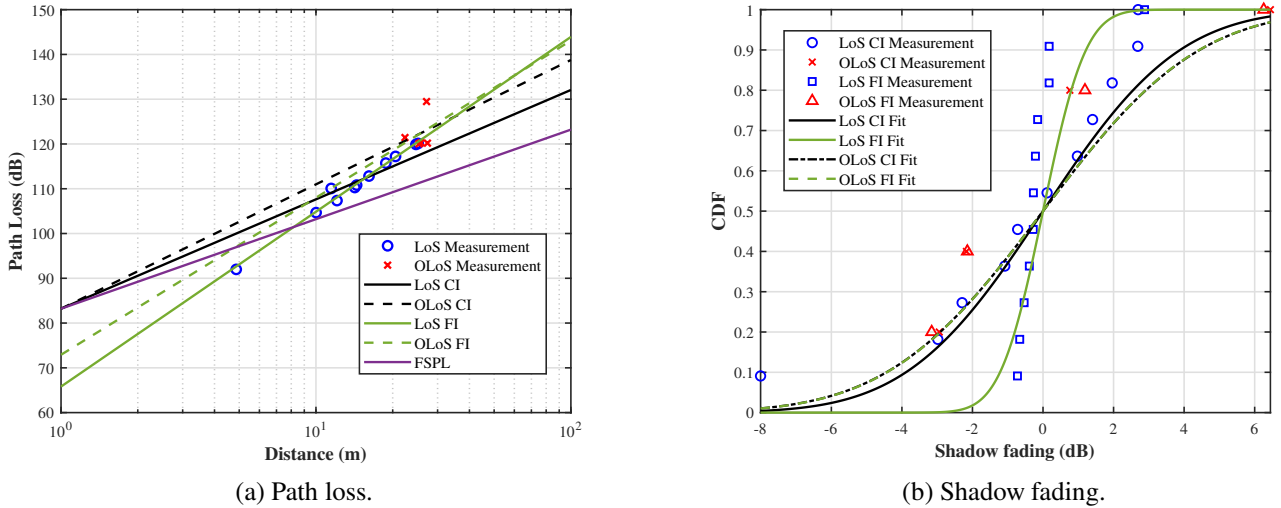


Fig. 5. Measured and fitted results for (a) path loss and (b) shadow fading.

### B. Path Loss and Shadow Fading

Based on Friis' transmission equation, the measurement results, and the system parameter settings, the received power can be calculated, from which the path loss is obtained. Specifically, the path loss in dB is computed as

$$PL = 10 \log_{10} \frac{P_t}{P_r} = -10 \log_{10} \left[ G_t G_r \left( \frac{\lambda_c}{4\pi d_{TR}} \right)^2 h \right], \quad (21)$$

where  $P_t$  (0.5 mW) and  $P_r$  denote the transmitted and received powers, respectively, and  $G_t$  (25 dBi) and  $G_r$  (25 dBi) denote the Tx and Rx antenna gains, respectively, and  $h = \sum_{k=1}^K APDP$ . The close-in (CI) model and the floating-intercept (FI) model are adopted to characterize the path loss and evaluate the most suitable path loss model for the measured outdoor scenario. The CI path loss model is given by

$$PL^{CI} = 10n \log_{10} \left( \frac{d_{TR}}{d_0} \right) + FSPL(f_c, d_0) + X_\sigma^{CI}, \quad (22)$$

where  $n$  is the path loss exponent (PLE), and  $d_0$  is the reference distance, which is set to 1 m in this scenario.  $X_\sigma^{CI}$  denotes the shadow fading term, which follows a zero-mean Gaussian distribution with standard deviation  $\sigma_{SF}^{CI}$ . The free-space path loss (FSPL) is given by

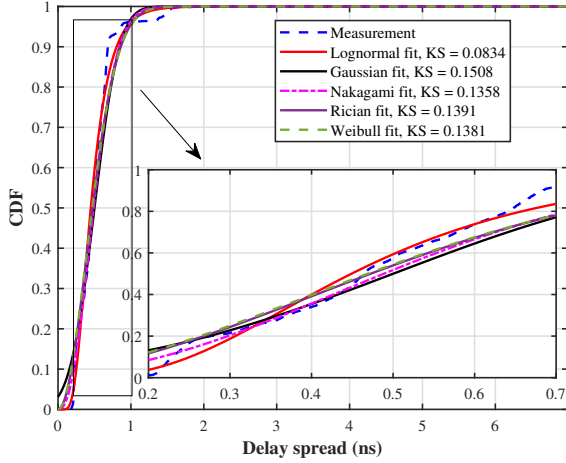
$$FSPL(f_c, d) = 20 \log_{10} \left( \frac{4\pi d f_c}{c} \right), \quad (23)$$

where  $c$  denotes the speed of light. Moreover, the FI path loss model is expressed as

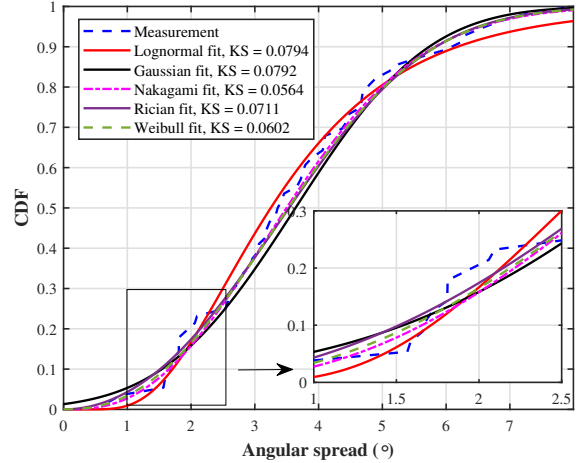
$$PL^{FI} = 10\alpha \log_{10} (d_{TR}) + \beta + X_\sigma^{FI}, \quad (24)$$

where  $\alpha$  and  $\beta$  denote the linear slope and floating intercept, respectively.  $X_\sigma^{FI}$  denotes the shadow fading term, which follows a zero-mean Gaussian distribution with standard deviation  $\sigma_{SF}^{FI}$ . The corresponding measurement and fitting results are presented in Fig. 5 and Table II.

As shown in Fig. 5 (a), relatively high PL values are expected in outdoor environments because the propagation distances are generally longer than those in indoor scenarios. In addition,



(a) Delay spread.



(b) Angular spread.

Fig. 6. Measured and fitted results for (a) delay spread and (b) angular spread.

obstruction effects further increase the PL under OLoS cases. For the CI model, the fitted PLEs are  $n_{\text{LoS}} = 2.443$  and  $n_{\text{OLoS}} = 2.778$ . Compared with the UMi street canyon path loss models in the millimeter-wave (mmWave) frequency bands summarized in [32], the obtained  $n_{\text{LoS}}$  is higher than the corresponding LoS reference values, whereas  $n_{\text{OLoS}}$  remains lower than the typical NLoS values. This is because the relatively large LoS PLE reflects additional propagation loss caused by the practical THz measurement environment, while the further increase in the OLoS case captures the extra attenuation introduced by vegetation blockage. Moreover, the FI model provides a better fit than the CI model. This improvement can be attributed to the flexibility of the FI model in jointly optimizing the intercept and slope, enabling it to better accommodate empirical variations without being constrained by a fixed reference distance.

As shown in Fig. 5 (b), the CI and FI models yield similar SF fitting results for the OLoS case. In the LoS case, however, the CI model provides a more suitable characterization of SF, with  $\sigma_{\text{SF,LoS}}^{\text{CI}} = 3.034$  dB, which is consistent with the UMi street canyon LoS scenario specified in 3GPP TR 38.901 [33]. In contrast, the FI model fits the PL data very closely in the LoS case, leaving only small residual variations and making the resulting SF distribution less physically interpretable. Therefore, the FI model is more suitable for empirical PL fitting, whereas the CI model provides a more physically meaningful basis for SF characterization.

### C. Delay and Angular spreads

The RMS DS is widely used to characterize delay dispersion in the channel and is calculated as

$$\sigma_{\tau} = \sqrt{\frac{\sum_{l=1}^L |\alpha_l|^2 \tau_l^2}{\sum_{l=1}^L |\alpha_l|^2} - \left( \frac{\sum_{l=1}^L |\alpha_l|^2 \tau_l}{\sum_{l=1}^L |\alpha_l|^2} \right)^2}. \quad (25)$$

Similarly, the RMS AS characterizes the dispersion of channel power across different angular directions and is given by

$$\sigma_{\omega} = \sqrt{\frac{\sum_{l=1}^L |\alpha_l|^2 \omega_l^2}{\sum_{l=1}^L |\alpha_l|^2} - \left( \frac{\sum_{l=1}^L |\alpha_l|^2 \omega_l}{\sum_{l=1}^L |\alpha_l|^2} \right)^2}. \quad (26)$$

The measurement and fitting results are shown in Table II and Fig. 6. To characterize and model the RMS DS and AS<sup>5</sup>, the empirical CDFs are fitted to various distributions, including Lognormal (LN), Gaussian, Nakagami, Rician, and Weibull. The KS test is then performed to assess the goodness of fit between the empirical CDFs and the candidate distributions. The distribution with the smallest KS distance is considered to provide the best fit. The DS fitting results shown in Fig. 6 (a) indicate that the LN distribution provides the best fit, which is consistent with the observation in [19]. For the AS, however, the Nakagami distribution yields the best fitting performance, with the fitted parameters  $m = 1.362$  and  $\Omega = 15.913$ . Nevertheless, the other candidate distributions also exhibit relatively low KS values, indicating that they can also provide reasonably good fits to the measured AS.

According to [33], for the UMi street canyon LoS scenario,  $\mu_{\text{DS}} = -0.24 \log_{10}(1 + f_c) - 7.14 \approx -7.749$  and  $\sigma_{\text{DS}} = 0.38$ . For the NLoS scenario,  $\mu_{\text{DS}} = -0.24 \log_{10}(1 + f_c) - 6.83 \approx -7.439$  and  $\sigma_{\text{DS}} = 0.16 \log_{10}(1 + f_c) + 0.28 \approx 0.686$ , where  $f_c$  denotes the carrier frequency in GHz. After converting the measured values from  $\log_{10}(\text{DS}/1\text{ns})$  to  $\log_{10}(\text{DS}/1\text{s})$ , the obtained  $\mu_{\text{DS}}$  is  $-9.348$ , which is smaller than the corresponding 3GPP UMi street canyon values. This difference is mainly because THz-band propagation experiences much stronger path loss, weaker diffraction, and poorer penetration than mmWave propagation. Consequently, weak long-delay MPCs are significantly suppressed, and the received power is mainly concentrated in the

<sup>5</sup>Due to the limited number of antenna elements at the Rx side and the lack of significant angular-domain information, the actual estimation is performed by traversing four Tx-side multiple-input single-output (MISO) systems to achieve high estimation accuracy, and only the AoD information  $\omega$  is analyzed.

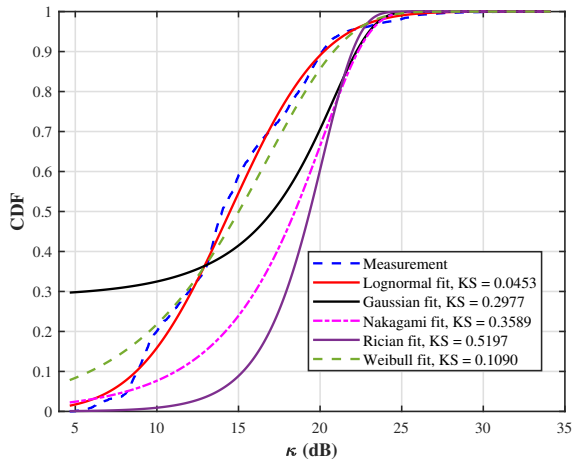


Fig. 7. Measured and fitted results for KF.

LoS path or a few strong specular components, resulting in a sparse multipath structure and a smaller RMS DS. The smaller  $\sigma_{DS}$  can be attributed to the limited measurement area and the spatial correlation among VAA samples.

Fig. 6 (b) shows the AS fitting results. According to [33], for the UMi street canyon LoS scenario,  $\mu_{AS} = -0.05 \log_{10}(1 + f_c) + 1.21 \approx 1.083$  and  $\sigma_{AS} = 0.41$ . For the NLoS scenario,  $\mu_{AS} = -0.23 \log_{10}(1 + f_c) + 1.53 \approx 0.946$  and  $\sigma_{AS} = 0.11 \log_{10}(1 + f_c) + 0.33 \approx 0.609$ . In contrast, the fitting results obtained in this measurement environment are  $\mu_{AS} = 0.512$  and  $\sigma_{AS} = 0.218$ , which are smaller than the corresponding 3GPP values. This indicates that the measured THz channel exhibits a more concentrated angular distribution. Such a result is consistent with the propagation characteristics in the THz-band discussed above. Although the overall AS is relatively small, clear differences can still be observed between LoS and OLoS links. The OLoS locations generally exhibit larger AS values than their adjacent LoS locations. For example,  $\sigma_\omega$  increases from  $2.418^\circ$  at TRx5 to  $4.353^\circ$  at TRx6, from  $1.732^\circ$  at TRx8 to  $3.187^\circ$  at TRx7, from  $4.288^\circ$  at TRx10 to  $5.651^\circ$  at TRx11, and from  $4.309^\circ$  at TRx14 to  $5.658^\circ$  at TRx13. This suggests that vegetation-induced blockage and obstruction effects increase the angular dispersion.

#### D. Rician K-factor

The Rician KF characterizes the power dominance of the strongest MPC relative to the remaining MPCs in the channel. It is defined as

$$\kappa = \frac{\max_{\tau} \text{APDP}_{\tau}}{\sum_{\tau} \text{APDP}_{\tau} - \max_{\tau} \text{APDP}_{\tau}}, \quad (27)$$

where  $\text{APDP}_{\tau}$  denotes the aggregated APDP power of MPCs with closely spaced delays. The 512 KF samples obtained at each TRx location are fitted using various distributions, and the corresponding results are presented in Table II and Fig. 7. The KS test results indicate that the LN distribution provides the best fit among the considered distributions.

In the outdoor scenario, the KF values are generally high. The overall LN-fitted KF parameters are  $\mu_{\kappa} = 14.48$  dB and

$\sigma_{\kappa} = 4.49$  dB, indicating a larger mean KF than the 3GPP UMi street canyon LoS value of 9 dB, while the standard deviation remains comparable to the 3GPP value of 5 dB. This difference is mainly attributed to the sparse propagation characteristics of the THz band, where the received power is predominantly concentrated in the dominant delay cluster, which typically corresponds to the LoS component. The relatively large  $\sigma_{\kappa}$  at TRx1 is caused by its near-field propagation condition. Since TRx1 lies within the Rayleigh distance of the VAA, the dominant path power varies significantly across the antenna aperture, leading to stronger spatial variations in the KF. In addition, OLoS locations generally exhibit larger  $\sigma_{\kappa}$  values than adjacent LoS locations, as observed by comparing TRx6 with TRx5, TRx7 with TRx8, TRx11 with TRx10, and TRx13 with TRx14. This is because vegetation obstruction introduces path visibility variations and makes the relative strength of the dominant cluster more sensitive to the antenna location.

#### E. Correlation Properties

The correlation coefficient between the  $(r, m)$ -th CIR  $\mathbf{c}^{(r,m)}$  and  $(r, n)$ -th CIR  $\mathbf{c}^{(r,n)}$  is defined as

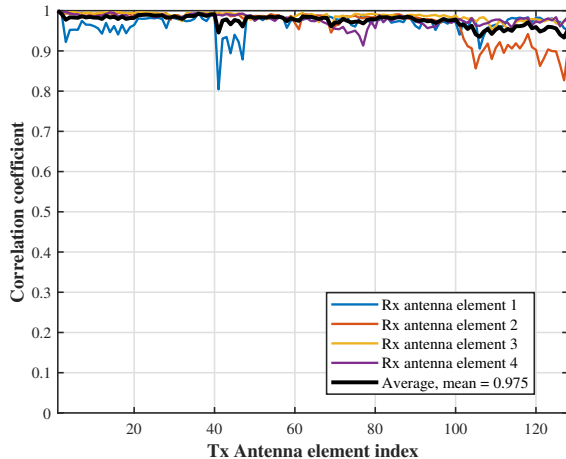
$$\rho_{m,n}^{(r)} = \frac{\mathbb{E} \left[ \left[ (\mathbf{c}^{(r,m)} - \bar{\mathbf{c}}^{(r,m)})^H (\mathbf{c}^{(r,n)} - \bar{\mathbf{c}}^{(r,n)}) \right] \right]}{\sqrt{\mathbb{E} \left[ \|\mathbf{c}^{(r,m)} - \bar{\mathbf{c}}^{(r,m)}\|_2^2 \right] \mathbb{E} \left[ \|\mathbf{c}^{(r,n)} - \bar{\mathbf{c}}^{(r,n)}\|_2^2 \right]}}, \quad (28)$$

where  $\bar{\mathbf{c}}^{(r,m)}$  and  $\bar{\mathbf{c}}^{(r,n)}$  denote the mean components of the corresponding CIRs. Fig. 8 shows the CIR correlation coefficients between the reference antenna location  $(r, 1)$  and the  $(r, n)$ -th antenna location for the four Rx antenna elements, as well as their average, at the TRx10 and TRx11 locations.

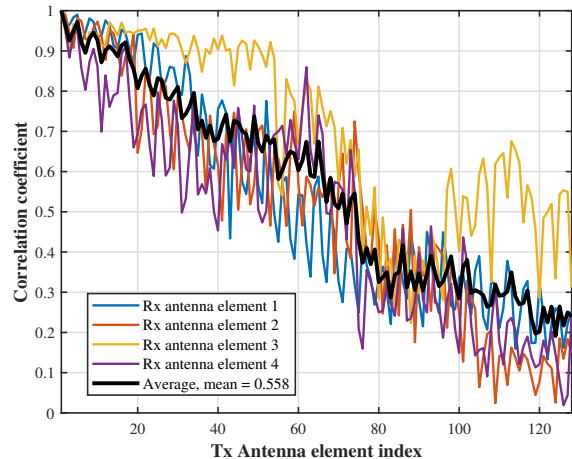
For the far-field LoS case at TRx10, the CIR correlation coefficients remain close to 1 across the entire VAA, indicating a highly spatially stationary channel dominated by a stable LoS component. This suggests that the channel responses observed at different antenna elements share similar delay-domain structures, and the dominant propagation path remains consistently visible over the array aperture. In contrast, the OLoS case at TRx11 exhibits an evident periodic decay in the CIR correlation coefficient as the antenna element index increases. This behavior indicates that the channel responses become increasingly dissimilar across antenna elements due to blockage-induced path visibility variations. Specifically, vegetation obstruction weakens or blocks the dominant component over part of the array aperture, while reflected or scattered components become relatively more significant, leading to stronger SnS. Therefore, compared with the far-field LoS case, the OLoS case exhibits more pronounced element-wise channel variation, suggesting that array-wide stationarity assumptions may be inaccurate for THz MIMO channels under blockage conditions.

#### F. Near-field effects

The Rayleigh distance for the considered VAA configuration is  $2D^2/\lambda_c = (N_T - 1)^2 \lambda_c / 2 \approx 7.013$  m. Therefore, TRx1 is located in the near-field region, whereas TRx4 is located in the far-field region. As shown in Fig. 9, we investigate the phase variations across the antenna element index for Rx antenna

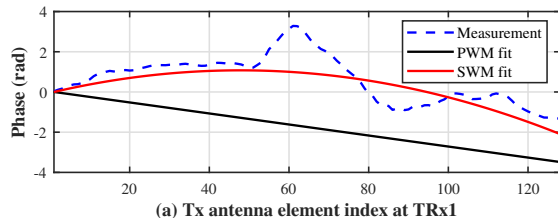


(a) TRx10.

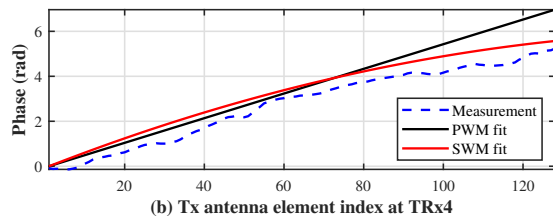


(b) TRx11.

Fig. 8. CIR correlation coefficients across the Tx antenna element index at (a) TRx10 (LoS) and (b) TRx11 (OLoS).



(a) Tx antenna element index at TRx1



(b) Tx antenna element index at TRx4

Fig. 9. Phase variations across the Tx antenna element index for Rx antenna element 2 at (a) TRx1 (near-field) and (b) TRx4 (far-field).

element 2 at TRx1 and TRx4. Since the LoS path does not involve interactions with scatterers, the observed phase variation is mainly determined by near-field propagation and possible beam misalignment effects [34]. Under the far-field plane wave model (PWM), the phase variation across antenna elements is expected to be approximately linear [35]. However, at TRx1, the measured phase response agrees more closely with the spherical wave model (SWM) [36], while exhibiting a clear deviation from the PWM. In contrast, at TRx4, the measured data are well fitted by both models, indicating that the plane wave approximation is valid in the far-field region.

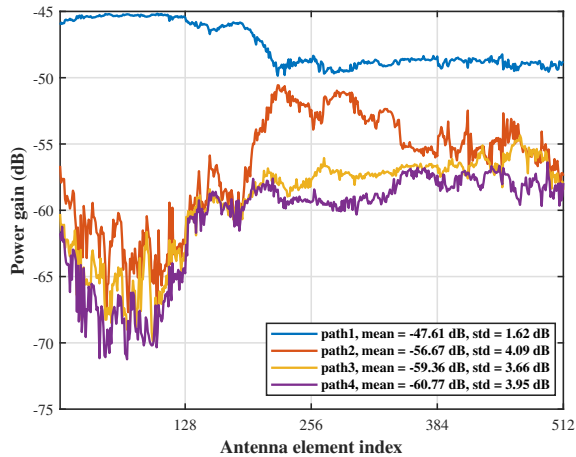
Notably, the measured phase does not follow an ideally smooth curve because the extracted dominant component is affected by practical measurement and propagation factors. In particular, beam misalignment, residual phase drift, path-association uncertainty in the SAGE estimation may perturb the measured phase response. Nevertheless, compared with

the linear phase response predicted by the PWM, the SWM better captures the nonlinear phase curvature of the measured response at TRx1, thereby confirming the near-field spherical-wave characteristics of the LoS component.

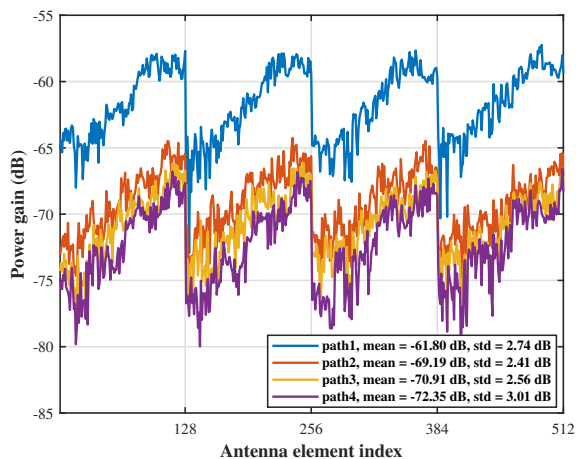
### G. MIMO Properties

1) *Spatial Non-stationary Characteristics*: We investigate the power-antenna element index profiles at different TRx locations, as shown in Fig. 10. The figure illustrates how the four paths with the highest average power vary across the antenna array. Specifically, the VAA element index ranges from 1 to 512, corresponding to four concatenated Rx blocks, each containing 128 Tx antenna locations. For each path, the mean and standard deviation are calculated to quantify its spatial power variation. The mean reflects the average power level of the path, whereas the standard deviation characterizes the degree of power fluctuation along the antenna array.

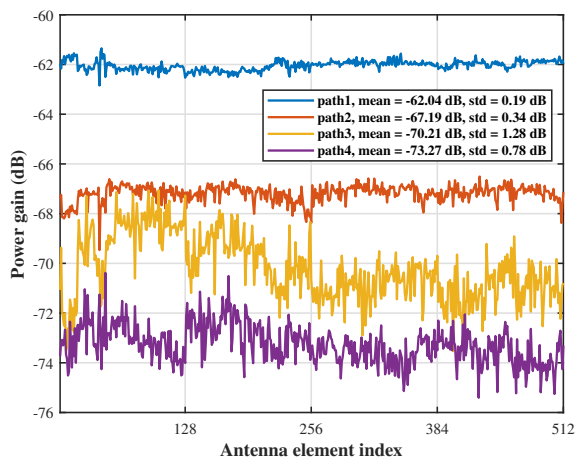
For TRx1, the path gains vary significantly across the VAA. In particular, the standard deviation of Path 2 reaches 4.09 dB, indicating strong spatial power fluctuation. This suggests that the near-field LoS component is not spatially stationary over the large array aperture, which can be attributed to spherical wave propagation and the limited visible region (VR). In contrast, TRx10 exhibits relatively stable path gains across the array, with small standard deviations for all four paths, since the LoS component lies in the far-field region. The dominant path remains nearly unchanged along the antenna index, while the weaker paths are clearly separated in power, as reflected by their mean values. For the OLoS case at TRx6, the path gains exhibit periodic variations along the stacked antenna index, and the relatively large standard deviations of all four paths indicate strong spatial fluctuations. Since the 512 indices are formed by concatenating four Rx blocks, this phenomenon is mainly caused by the fact that the obstruction effect is more sensitive to variations in the Tx antenna elements, whereas the Rx antenna elements are few in number and located within approximately the same geometric obstruction region.



(a) TRx1.



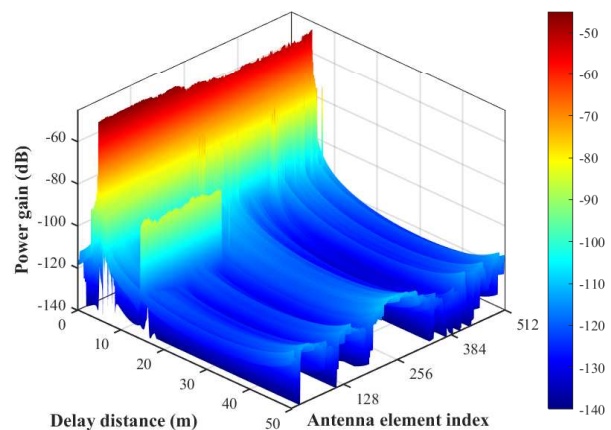
(b) TRx6.



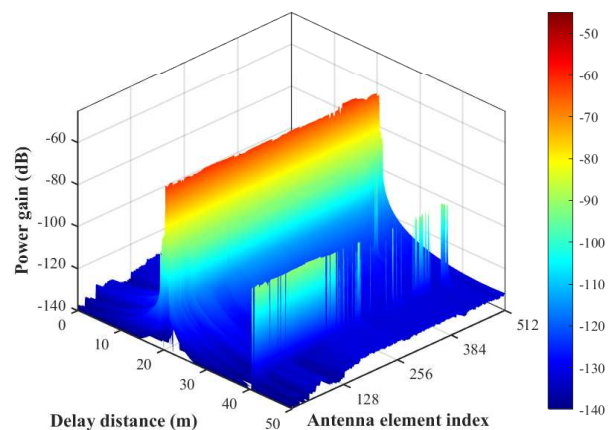
(c) TRx10.

Fig. 10. Power-antenna element index profiles at (a) TRx1 (LoS, near-field), (b) TRx6 (OLOs, far-field), and (c) TRx10 (LoS, far-field).

2) *Cluster Birth-Death Property*: Fig. 11 (a) and Fig. 11 (b) show the cluster birth-death property of the PDPs along the



(a) TRx1.



(b) TRx4.

Fig. 11. Power-delay-antenna element index profiles at (a) TRx1, and (b) TRx4.

antenna element index at the TRx1 and TRx4 locations, respectively. Some high-order reflected MPCs, such as the component around 15 m at TRx1 and the component around 40 m at TRx4, are only visible over a limited range of antenna elements rather than across the entire VAA.

This phenomenon indicates that certain scattering clusters do not contribute to all antenna elements. Instead, they appear and disappear along the array axis. In the figure, these clusters form discontinuous ridge-like segments over specific antenna-index ranges. The starting point of each segment corresponds to the birth of a cluster, while the endpoint corresponds to its death. Therefore, the observed high-order reflected MPCs exhibit clear cluster birth-death behavior. These results verify the existence of cluster birth-death characteristics in THz-band MIMO channels, which can be mainly attributed to the limited VR of scatterers. For example, at TRx1, Rx1 is approximately located within the VR of the reflected cluster, whereas the other Rx positions are outside this region. This observation further demonstrates that THz-band multipath propagation exhibits non-stationary power variations and cluster evolution along the array aperture. Therefore, non-stationary effects should be considered in THz-

band MIMO channel modeling [30].

## V. CONCLUSION

In this paper, we conducted a 330-360 GHz channel measurement campaign in an outdoor UMi street canyon scenario using a  $128 \times 4$  VAA-based MIMO configuration. The environmental stationarity was verified, and a PD-aware SAGE algorithm was proposed for measurement data post-processing, which improves both delay resolution and channel parameter estimation accuracy. Based on the processed data, the channel characteristics of LoS and OLoS links were analyzed and modeled. The results showed that outdoor THz-band propagation exhibits distinct characteristics compared with mmWave bands, particularly in terms of PL, SF, DS, AS, KF, and correlation properties. Statistical fitting was further performed for key channel parameters, and the KS test was used to evaluate the goodness of fit between the empirical CDFs and candidate distributions. Near-field effects and MIMO-specific features, including SnS and cluster birth-death property, were also investigated. The comparative analysis between LoS and OLoS links revealed the impact of vegetation obstruction on outdoor THz propagation characteristics.

## REFERENCES

- [1] C.-X. Wang *et al.*, “6G wireless channel measurements and models: Trends and challenges,” *IEEE Veh. Technol. Mag.*, vol. 15, no. 4, pp. 22–32, Oct. 2020.
- [2] C. Han *et al.*, “Terahertz wireless channels: A holistic survey on measurement, modeling, and analysis,” *IEEE Commun. Surveys Tuts.*, vol. 24, no. 3, pp. 1670–1707, Jun. 2022.
- [3] Y. J. Guo, C. A. Guo, M. Li, and M. Latva-Aho, “Antenna technologies for 6G—advances and challenges,” *IEEE Trans. Antennas Propag.*, vol. 74, no. 5, pp. 3865–3880, 2026.
- [4] J. Zhang *et al.*, “Channel measurement, modeling, and simulation for 6G: A survey and tutorial,” *arXiv preprint arXiv:2305.16616*, 2023.
- [5] D. Serghiou, M. Khalily, T. W. C. Brown, and R. Tafazolli, “Terahertz channel propagation phenomena, measurement techniques and modeling for 6G wireless communication applications: A survey, open challenges and future research directions,” *IEEE Commun. Surveys Tuts.*, vol. 24, no. 4, pp. 1957–1996, Sept. 2022.
- [6] T. S. Rappaport *et al.*, “Wireless communications and applications above 100 GHz: Opportunities and challenges for 6G and beyond,” *IEEE Access*, vol. 7, pp. 78 729–78 757, Jun. 2019.
- [7] S. Ju *et al.*, “142 GHz sub-terahertz radio propagation measurements and channel characterization in factory buildings,” *IEEE Trans. Wireless Commun.*, vol. 23, no. 7, pp. 7127–7143, Jul. 2024.
- [8] Y. Chen, C. Han, Z. Yu, and G. Wang, “Channel measurement, characterization, and modeling for terahertz indoor communications above 200 GHz,” *IEEE Trans. Wireless Commun.*, vol. 23, no. 6, pp. 6518–6532, Jun. 2024.
- [9] Y. Wang, X. Zhou, X. Liao, J. Zhang, and J. Zhang, “Channel measurements and multipath characterization for indoor sub-terahertz communication,” *IEEE Trans. Veh. Technol.*, vol. 74, no. 3, pp. 4393–4407, Mar. 2025.
- [10] T. Zhang *et al.*, “Indoor channel measurements and characterization for virtual multi-antenna at 260 GHz to 400 GHz,” *IEEE Antennas Wireless Propag. Lett.*, vol. 24, no. 11, pp. 3841–3845, Nov. 2025.
- [11] T. Doeker, J. M. Eckhardt, and T. Kürner, “Channel measurements and modeling for low terahertz communications in an aircraft cabin,” *IEEE Trans. Antennas Propag.*, vol. 70, no. 11, pp. 10903–10916, Nov. 2022.
- [12] X. Liao, H. Tang, X. Zheng, X. Hao, and Y. Wang, “Channel measurements, characterization and performance analysis for an aircraft cabin from mmwave to sub-THz communication,” *IEEE Trans. Veh. Technol.*, pp. 1–14, Feb. 2026.
- [13] K. Guan *et al.*, “Channel characterization and capacity analysis for THz communication enabled smart rail mobility,” *IEEE Trans. Veh. Technol.*, vol. 70, no. 5, pp. 4065–4080, May 2021.
- [14] G. Liu *et al.*, “Impact of snowfall on terahertz channel performance: Measurement and modeling insights,” *IEEE Trans. THz Sci. Technol.*, vol. 14, no. 5, pp. 691–698, Sep. 2024.
- [15] S. Ju and T. S. Rappaport, “140 GHz urban microcell propagation measurements for spatial consistency modeling,” in *Proc. IEEE Int. Conf. Commun. (ICC)*, Jun. 2021, pp. 1–6.
- [16] Y. Xing and T. S. Rappaport, “Propagation measurements and path loss models for sub-THz in urban microcells,” in *Proc. IEEE Int. Conf. Commun. (ICC)*, Jun. 2021, pp. 1–6.
- [17] S. Ju and T. S. Rappaport, “Sub-terahertz spatial statistical MIMO channel model for urban microcells at 142 GHz,” in *Proc. IEEE Global Commun. Conf. (GLOBECOM)*, Dec. 2021, pp. 1–6.
- [18] D. Shakya *et al.*, “Radio propagation measurements and statistical channel models for outdoor urban microcells in open squares and streets at 142, 73, and 28 GHz,” *IEEE Trans. Antennas Propag.*, vol. 72, no. 4, pp. 3580–3595, Apr. 2024.
- [19] A. Al-jzari, Y. He, J. Hu, and S. Salous, “Sub-THz and THz channel measurements and characteristic analysis in indoor and outdoor environments for 6G wireless systems,” *IEEE Trans. THz Sci. Technol.*, vol. 15, no. 6, pp. 976–984, Nov. 2025.
- [20] Y. Wang, Y. Lil, Y. Chen, Z. Yu, and C. Han, “Terahertz channel measurement and analysis on a university campus street,” in *Proc. IEEE Int. Conf. Commun. (ICC)*, May 2023, pp. 2075–2080.
- [21] N. A. Abbasi *et al.*, “THz band channel measurements and statistical modeling for urban D2D environments,” *IEEE Trans. Wireless Commun.*, vol. 22, no. 3, pp. 1466–1479, Mar. 2023.
- [22] N. A. Abbasi *et al.*, “THz band channel measurements and statistical modeling for urban microcellular environments,” *IEEE Trans. Wireless Commun.*, vol. 23, no. 7, pp. 6719–6734, July 2024.
- [23] J. Huang *et al.*, “Multi-frequency mmwave massive MIMO channel measurements and characterization for 5G wireless communication systems,” *IEEE J. Sel. Areas Commun.*, vol. 35, no. 7, pp. 1591–1605, July 2017.
- [24] D. Baum and H. Bolcskei, “Impact of phase noise on MIMO channel measurement accuracy,” in *Proc. IEEE Vehicular Technology Conference (VTC-Fall)*, vol. 3, Sept. 2004, pp. 1614–1618.
- [25] A. Taparugssanagorn and J. Ylitalo, “Characteristics of short-term phase noise of MIMO channel sounding and its effect on capacity estimation,” *IEEE Trans. Instrum. Meas.*, vol. 58, no. 1, pp. 196–201, Jan. 2009.
- [26] V. Kristem *et al.*, “3D MIMO outdoor-to-indoor propagation channel measurement,” *IEEE Trans. Wireless Commun.*, vol. 16, no. 7, pp. 4600–4613, July 2017.
- [27] J. Fessler and A. Hero, “Space-alternating generalized expectation-maximization algorithm,” *IEEE Trans. Signal Process.*, vol. 42, no. 10, pp. 2664–2677, Oct. 1994.
- [28] B. Fleury, M. Tschudin, R. Heddergott, D. Dahlhaus, and K. Ingeman Pedersen, “Channel parameter estimation in mobile radio environments using the SAGE algorithm,” *IEEE J. Sel. Areas Commun.*, vol. 17, no. 3, pp. 434–450, Mar. 1999.
- [29] Y. Wang, S. Sun, and C. Han, “Far- and near-field channel measurements and characterization in the terahertz band using a virtual antenna array,” *IEEE Commun. Lett.*, vol. 28, no. 5, pp. 1186–1190, May 2024.
- [30] H. Xu *et al.*, “Empirical study on near-field and spatial non-stationarity modeling for THz XL-MIMO channel in indoor scenario,” *IEEE Trans. Wireless Commun.*, vol. 25, pp. 4435–4451, Sep. 2026.
- [31] M. Li, F. Zhang, Y. Lyu, Z. Yuan, and W. Fan, “Antenna deembedding in directional channel measurements with virtual array concept and experimental validation,” *IEEE Trans. Antennas Propag.*, vol. 72, no. 1, pp. 1063–1068, Jan. 2024.
- [32] T. S. Rappaport *et al.*, “Overview of millimeter wave communications for fifth-generation (5G) wireless networks—with a focus on propagation models,” *IEEE Trans. Antennas Propag.*, vol. 65, no. 12, pp. 6213–6230, Dec. 2017.
- [33] 3GPP, “Study on channel model for frequencies from 0.5 to 100 GHz,” 3rd Generation Partnership Project (3GPP), Technical Report (TR) 38.901 version 17.0.0, Apr. 2022.
- [34] H. Xu *et al.*, “An empirical study on near-field, spatial non-stationarity, and beam misalignment characteristics of THz XL-MIMO channels at 132 GHz,” in *Proc. IEEE Int. Conf. Commun. Workshops (ICC Workshops)*, Jun. 2024, pp. 744–749.
- [35] Z. Yuan, J. Zhang, Y. Ji, G. F. Pedersen, and W. Fan, “Spatial non-stationary near-field channel modeling and validation for massive MIMO systems,” *IEEE Trans. Antennas Propag.*, vol. 71, no. 1, pp. 921–933, Jan. 2023.
- [36] P. Wang, Y. Li, X. Yuan, L. Song, and B. Vucetic, “Tens of gigabits wireless communications over E-band LoS MIMO channels with uniform linear antenna arrays,” *IEEE Trans. Wireless Commun.*, vol. 13, no. 7, pp. 3791–3805, Jul. 2014.